Structure and Properties of Nanosilicates with Olivine (Mg₂SiO₄)ₙ and Pyroxene (MgSiO₃)ₙ Compositions

Antoni Macià Escatllar,[†] Tomas Lazaukas,[‡] Scott M. Woodley,*,[‡] and Stefan T. Bromley*,[†,§]

[†]Departament de Ciència de Materials i Química Física & Institut de Química Teòrica i Computacional (IQTCUB), Universitat de Barcelona, E-08028 Barcelona, Spain

[‡]Department of Chemistry, University College, London WC1H 0AJ, U.K.

[§]Institució Catalana de Recerca i Estudis Avançats (ICREA), E-08010 Barcelona, Spain

Ⓢ *Supporting Information*

ABSTRACT: Magnesium-rich silicates are ubiquitous both terrestrially and astronomically, where they are often present as small particles. Nanosized Mg-rich silicate particles are likely to be particularly important for understanding the formation, processing, and properties of cosmic dust grains. Although astronomical observations and laboratory studies have revealed much about such silicate dust, our knowledge of this hugely important class of nanosolids largely rests on top-down comparisons with the properties of bulk silicates. Herein, we provide a foundational bottom-up study of the structure and properties of Mg-rich nanosilicates based on carefully procured atomistic models. Specifically, we employ state-of-the-art global optimization methods to search for the most stable structures of silicate nanoclusters with olivine (Mg₂SiO₄)ₙ and pyroxene (MgSiO₃)ₙ compositions with $N = 1-10$. To ensure the reliability of our searches, we develop a new interatomic potential that has been especially tuned for nanosilicates. Subsequently, we refine these searches and calculate a range of physicochemical properties of the most stable nanoclusters using accurate density functional theory based electronic structure calculations. We report a detailed analysis of structural and energy properties, charge distributions, and infrared vibrational spectra, where in all cases we compare our finding for nanosilicates with those of the corresponding bulk silicate crystals. For most properties considered, we find large differences with respect to the bulk limit, underlining the limitations of a top-down approach for describing these species. Overall, our work provides a new platform for an accurate and detailed understanding of nanoscale silicates.

KEYWORDS: *cosmic dust grains, silicates, infrared spectra, nanoclusters, interstellar medium, computational modeling, global optimization, density functional theory*
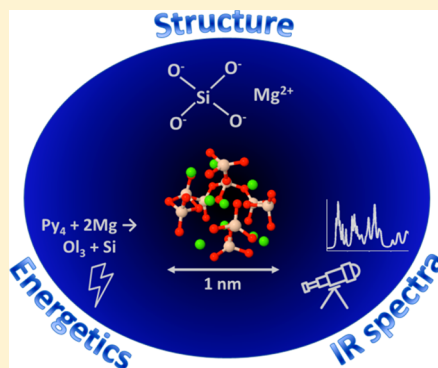
INTRODUCTION

Silicates constitute the largest fraction of solid matter in the universe. Although bulk silicates form the basis for the geology of the earth's crust and mantle,[1] weathering processes produce mineral nanoparticles which are widely distributed throughout many terrestrial systems.[2] Tonnes of small silicate particles also enter our atmosphere every day in the form of interplanetary dust particles.[3] Indeed, all planetary silicates have their origin in such extraterrestrial silicate dust, which is ubiquitously found in numerous astronomical environments.[4,5] Much of this silicate cosmic dust is formed around evolved oxygen-rich stars where it nucleates from small nanoscale clusters to form micrometer-sized grains, which are then injected into the interstellar medium (ISM).[6] Before their eventual coalescence into larger bodies in protoplanetary disks, these grains follow a long and tumultuous journey through the ISM. During this time the dust is subject to processing by high-energy particles and radiation (e.g., fragmentation, destruction, and reformation), leading to silicates with a range of sizes, shapes, chemical

compositions, and structures.[7,8] Largely because of such processes, a significant percentage of silicate cosmic dust grains are likely to be nanosized (i.e., with diameters of between 1 and 100 nm). Using observational constraints, it has been estimated that up to 10% of the mass fraction of silicate grains in the ISM could form a large population of very small nanosilicates with diameters of less than 3 nm.[9] We also note that the modeling of brown dwarf atmospheres also underlines the likely importance of (nano)silicates in cloud formation and the temperatures of such objects.[10,11]

Clues to the chemical structures and composition of silicate dust in astronomical environments largely rely on the fact that silicates tend to absorb and/or emit light at two characteristic infrared (IR) wavelengths around 10 and 20 μm, which are

associated with vibrational modes associated with Si−O stretching and O−Si−O bending, respectively. A comparison of IR observations with spectra from laboratory silicate samples has generally confirmed that cosmic silicates are probably of pyroxene ($Mg_{1-n}Fe_nSiO_3$) or olivine ($Mg_{2-n}Fe_nSiO_4$) compositions or mixtures thereof and are very Mg-rich.[12] In some specific cases, crystalline grains of these two compositions (i.e., enstatite and forsterite, respectively, for the Mg-rich end members) have been observed; however, in the majority of cases, the observed IR spectra exhibit only two broad silicate peaks, and no detailed chemical structural information can be obtained. As such, the available information on the properties of nanoscale silicates is very limited.

Herein, we provide the structures and properties of stable Mg-rich pyroxene ($(MgSiO_3)_N$) and olivine ($(Mg_2SiO_4)_N$) nanosilicates for $N = 1-10$ (~0.4−1.1 nm diameters) with structures obtained via global optimization searches and properties evaluated using accurate quantum chemical calculations. We analyze how the structure and properties of nano-olivines and nano-pyroxenes evolve with size and how both compare with one another and their respective bulk crystalline limits. For example, by comparing the stabilities of these mixed magnesium silicate nanosystems with those of pure magnesium oxide ($(MgO)_N$) and silica ($(SiO_2)_N$) nanoclusters, we obtain nanosize-scaled formation energies, which are compared with those of the respective bulk phases. For all of our nanosilicates, we also calculate their IR spectra over a 5−25 μm wavelength range and compare them with typical IR spectra of astronomical silicate dust and of crystalline enstatite and forsterite. In general, our systematic and detailed study reveals a number of significant differences between nanosilicates and bulk silicates and provides a new platform for understanding the stabilities, structures, and properties of silicates from the nanoscale upwards.

■ METHODOLOGY

For both Mg-rich pyroxene ($(MgSiO_3)_N$) and olivine ($(Mg_2SiO_4)_N$) compositions, we employed global optimization methods to explore the potential energy surface (PES) of nanosilicate structures to find the lowest-energy isomers for each size for $N = 1-10$. For these calculations, we developed a specifically tailored interatomic potential (IP) for silicate nanoclusters and performed searches using both the Monte Carlo basin hopping (MCBH)[13] method and a genetic algorithm (GA),[14] as described below. Depending on the system size, 50 to 200 of the lowest-energy nanocluster isomers from the combined global optimization searches for each N and stoichiometry were then optimized without symmetry constraints using quantum chemical density functional theory (DFT)-based calculations. For the latter, we employed all-electron, full potential electronic structure code FHI-aims[15] using the PBE0 hybrid functional[16] and a Tier1/light-atom-centered numerical basis set. We note that the basis set has an accuracy comparable to that of a TZVP Gaussian-type orbital basis set.[17] DFT calculations of this type were used to derive all reported energies, charges, structures, and harmonic IR vibrational frequencies. All results pertain to the best global minimum (GM) candidate nanoclusters as determined by their lowest energy obtained via these DFT-based calculations.

Monte Carlo Basin Hopping (MCBH). Although originally applied to biomolecules,[18] the MCBH algorithm has been shown to be an excellent tool for exploring the low-energy PES of nanoclusters.[13] Our present application of the

method follows previous successful work on anhydrous and hydroxylated silica nanoclusters,[19−21] titanosilicate nanoclusters,[22] and the nucleation of silicon monoxide[23] and magnesium silicates.[24] The standard MCBH algorithm moves on the PES of nanocluster configurations through repeated steps of distorting optimized structures, through the application of small random atomic displacements, followed by structural reoptimization. To better explore the PES in our MCBH searches, in addition to atomic displacements, we also set 0.5% of the steps to attempt a Mg ↔ Si cation exchange move to further disrupt the nanocluster structure. After each step, newly optimized nanocluster structures are accepted if they are lower in energy than the previously accepted optimized structure. If they are higher in energy, then a probabilistic Metropolis criterion is employed to determine the outcome. In the latter, the probability of acceptance is lower/higher for a larger/smaller increase in energy. Herein, we employ our cascade MCBH code[25] which was written using the Python-based Atomistic Simulation Environment (ASE)[26] and which uses the General Utility Lattice Package (GULP)[27] code as an externally called nanocluster optimizer. The IPs we employ describe the polarizability of the oxygen anions through the core−shell model.[28] Highly distorted structures possessing polarized ions described in this way can be difficult to optimize. To avoid these difficulties, our cascade MCBH approach first optimizes distorted nanoclusters with a simplified IP without shells, followed by a more refined optimization with shells incorporated. For each nanocluster composition and size, we used 5 MCBH runs of between 10 000 and 250 000 steps depending on the cluster size and with each initialized using a distinct nanocluster structure. During each run, the temperature was dynamically adapted to maintain a target acceptance/rejection ratio of 0.65.

Genetic Algorithm (GA). A Lamarckian GA search of the PES of all nanocluster compositions and sizes was also performed using the Knowledge Led Master Code (KLMC)[14,29] software suite. The KLMC's GA module has previously been proven to efficiently locate low-energy minima for a range different systems.[30−33] Most of the search parameters were kept as defined in ref.[14] Some minor adjustments were, however, introduced in order to ensure a sufficiently intensive search of the PES for magnesium silicate nanoclusters. Namely, depending on the system size under investigation, the population size, number of iterations, and simulation box size were varied from 100 to 200, from 1000 to 2000, and from 10 to 28 Å, respectively. For each nanocluster size and stoichiometry (olivine and pyroxene), we performed five independent GA searches. We stopped our GA simulations when the energy of the lowest-energy structure and the average energy of the 20 lowest energy structures became stable.

Interatomic Potentials (IP). To make the application of both global optimization algorithms efficient and tractable for available computer resources when performing an extensive search of the PES for each nanocluster composition, IPs based on simple analytical expressions were used. Such IPs are computationally very inexpensive to evaluate with respect to quantum mechanical-based electronic structure calculations. Generally, however, IPs are parameterised to describe bulk crystalline systems and are thus often less reliable for describing nanoscale systems where structures can be more varied and disordered. Also, because they possess two types of cations, ternary magnesium silicate nanoclusters have a relatively high degree of configurational structural freedom

compared to clusters of binary ionic compounds. For any one nanocluster size with a fixed composition, for example, we can imagine a range of Mg/Si cationic ordering possibilities, ranging from various highly segregated structures (e.g., layered, core−shell, side-by-side) to fully mixed structures. Thus, in order to help our global optimization searches find low-energy isomers of $(Mg_2SiO_4)_N$ and $(MgSiO_3)_N$ nanoclusters we require an IP that provides a reasonably reliable description of the complex PES of these systems.

Herein, we have reparametrized a bulk-parametrized IP to more accurately describe the structures and energetics of nanosilicates. This strategy has previously been shown to work successfully in an IP-based global optimization study of silica nanoclusters.[34] Recently, we showed that FFSiOH[35] is a highly accurate and reliable bulk-parametrized IP for describing the structure and properties of hydroxylated silica nanoclusters.[36] Using the Si−O interaction in FFSiOH as a base, we incorporated new parameters to describe the Mg−O interaction in magnesium silicate nanoclusters based on a modified version of the Mg−O interaction potential used in a previously reported IP.[37] We refer to this new IP as Mg-FFSiOH, which incorporates a short-range Buckingham interaction, long-range electrostatics, and polarization of the oxygen anions:

$$U = \sum_i \sum_{j>i} \frac{q_i q_j}{r} + \frac{1}{2} \sum_O k^O_{C-S}(r^O_S - r^O_C)^2$$
$$+ \sum_a \left(A_a \exp\left(-\frac{r}{\rho_a}\right) - \frac{C_a}{r^6} \right)$$
$$+ \sum_b D_b[(1 - \exp(-a_b(r - r_b)))^2]$$

The full set of IP parameters for Mg-FFSiOH is provided in Table S1 of the Supporting Information (SI). Although our global optimization searches were mainly carried out using the Mg-FFSiOH IP, we also employed an IP used to model bulk crystalline olivine by Walker et al.[38] (hereafter referred to as IP-1) and an IP based on parameters published in ref 39 for pure Si−O and O−O interactions and parameters reported in a library file of the GULP code[27] for the Mg−O interaction (hereafter referred to as IP-2). The use of multiple IPs helped to provide a greater degree of structural richness to our searches. An example of the ability of Mg-FFSiOH to describe the relative energies of silicate nanoclusters with respect to those calculated by (DFT-based calculations is shown in Figure 1 for the cases of olivine $(Mg_2SiO_4)_6$ nanocluster isomers and $(MgSiO_3)_7$ pyroxene nanocluster isomers. In each case, we plot the Mg-FFSiOH-optimized energies versus the corresponding DFT-optimized energies for over 1000 distinct isomers obtained from global optimization searches. For the $(Mg_2SiO_4)_6$ searches we used Mg-FFSiOH and IP-1, and for the $(MgSiO_3)_7$ searches we used Mg-FFSiOH and IP-2. Clearly, in both cases, the Mg-FFSiOH calculated isomer energies correlate quite well with those from DFT-based calculations. For $(Mg_2SiO_4)_6$, the two lowest-energy isomers according to Mg-FFSiOH are also the lowest in energy for DFT. For $(MgSiO_3)_7$, the best GM candidate according to DFT is the 16th lowest-energy isomer with respect to Mg-FFSiOH. We note that our best GM candidates for both olivine and pyroxene nanoclusters for nearly all cases for $N > 5$ resulted from global optimization searches using Mg-FFSiOH.
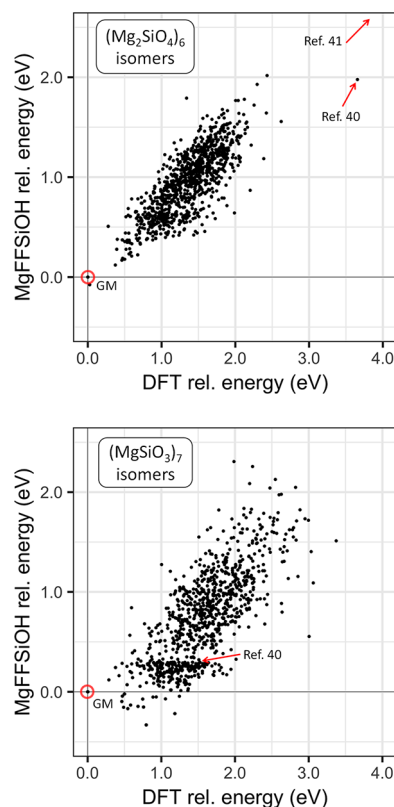

Figure 1. MgFFSiOH IP-optimized energies against DFT-optimized energies with respect to the energy of the lowest-energy DFT structure (GM) for ∼1000 isomers as obtained from global optimization searches described above for $(Mg_2SiO_4)_6$ olivine nanocluster isomers (upper) and $(MgSiO_3)_7$ pyroxene nanocluster isomers (lower). Data points corresponding to the GM candidates obtained in ref 40 are highlighted in each case. Note that the GM $(Mg_2SiO_4)_6$ candidate from ref 41 was found to lie over 5.5 eV higher in energy than our proposed GM isomer (as calculated via DFT) and is outside of the plotted range.

■ RESULTS AND DISCUSSION

Previous work by Woodley[40] using an evolutionary algorithm and a simplified version of IP-2 without polarizable shells on the oxygen anions was the first to report GM candidates for magnesium silicate nanoclusters. In this work, only IP-optimized nanocluster structures were reported (i.e., no DFT-based refinement, as performed in the present work) for $(Mg_2SiO_4)_N$ for $N = 1−7$ and for $(MgSiO_3)_N$ for $N = 1−10$. In ref 40, the GM candidates found for both olivine and pyroxene nanosilicate families were found to exhibit all or most of their Si cations in a single central network of oxygen-bridged SiO_4 tetrahedra decorated by peripherally scattered Mg cations. Only the larger $(Mg_2SiO_4)_N$ olivinic nanoclusters ($N = 4−7$) were found to display one SiO_4 unit separated from the main silica network. For the pyroxene $(MgSiO_3)_N$ GM candidates, the silica networks tended to be quite compact and form a number of $(SiO)_x$ rings with $x = 2−5$. A number of the predicted GM candidates displayed fairly symmetric structures and often displayed five-coordinate Si centers.

A more recent study by Mauney and Lazzati[41] focusing on the nucleation of astrophysical Mg-rich olivinic dust also derived some GM candidates for $(Mg_2SiO_4)_N$ with $N = 2−13$ using an IP (hereafter referred to as IP-3) which was derived from combining parameters from various sources.[34,37,42] The

reported Mg-rich olivine nanoclusters, like many of those in ref 40, possess a single ⋯Si−O⋯ bonded network. However, in ref 41 the reported lowest-energy nanoclusters have a relatively high degree of segregation. In particular, the silica fraction of the $(Mg_2SiO_4)_N$ nanoclusters was typically found to form highly compact subclusters sandwiched between dense MgO regions.

IP-2 and IP-3 have a number of parameters in common with IP-1. In fact, IP-1, IP-2, and IP-3 have a core set of parameters for O−O and Si−O interactions that can be found in earlier published IPs (e.g., refs 42 and 39). As such, we may expect that the reliabilities of the predicted low-energy isomers using each of these three IPs with respect to DFT-based calculations would be quite similar. In section S1 of the SI, we plot the relative energies of the 1000 $(Mg_2SiO_4)_6$ isomers in Figure 1 calculated using IP-1, IP-2, and IP-3 with respect to those calculated using DFT. Figure S2 shows that the performance of IP-1, IP-2 and IP-3 is rather poor compared to that of Mg-FFSiOH (Figure 1). The energetic stabilities of the candidate GM isomers for $(Mg_2SiO_4)_6$ proposed in ref 40 (using IP-2 without shells) and ref 41 (using IP-3) are also indicated in Figure 1 (upper). These isomers are found to be between 1.5 and 5.5 eV higher in energy (as calculated using DFT) than our GM candidate and to be less energetically stable than many other isomers in our extensive data set. The predicted GM isomer for $(MgSiO_3)_7$ in ref 40 is also highlighted in Figure 1 (lower), confirming the relatively worse performance of IP-2 for pyroxene nanoclusters. A more extensive comparison between IP-2 and DFT relative energies for $(MgSiO_3)_7$ isomers is reported in section S2 of the SI. Clearly, these comparisons raise serious doubts as to the adequacy of IP-1, IP-2, and IP-3 for finding structures of low-energy silicate nanoclusters.

Our newly parametrized Mg-FFSiOH, as employed herein, appears to provide a reasonably accurate and computationally efficient means to search the PES of energetically stable nanosilicate cluster structures. The use of a more accurate IP for our global optimizations with respect to previous searches is also clearly reflected in the structures of the resultant candidate GM nanocluster isomers. For example, in contrast to previous studies, the olivinic $(Mg_2SiO_4)_N$ nanocluster structures from our Mg-FFSiOH-based global optimization searches display increasingly nonsegregated structures with increasing size. This relatively low degree of SiO_4 polymerization in our olivine nanoclusters is consistent with the bulk crystalline phase of Mg_2SiO_4 (i.e., forsterite), where all of the silica tetrahedra are completely isolated. Below we provide a more detailed structural analysis of all of our GM nanocluster candidates followed by an evaluation of their charge distributions, energetics, and IR spectra.

Structure. Figures 2 and 3 show our candidate GM nanocluster structures for Mg-rich olivine $(Mg_2SiO_4)_N$ and pyroxene $(MgSiO_3)_N$ nanoclusters, respectively. Hereafter, we will refer to our olivine and pyroxene nanoclusters with N units by the abbreviations O-N and P-N, respectively. The Cartesian coordinates of the atoms in all nanoclusters are provided in the SI and are also available in the open access HIVE database of atomic structures for nanoclusters (https://hive.chem.ucl.ac.uk/).

Although the majority of the O-N and P-N nanocluster structures are nonsymmetric, a few symmetric and nearly symmetric cases were found. For olivine nanoclusters, symmetry is exhibited only by O-1 (C_{2v}) and O-2 (C_s). The
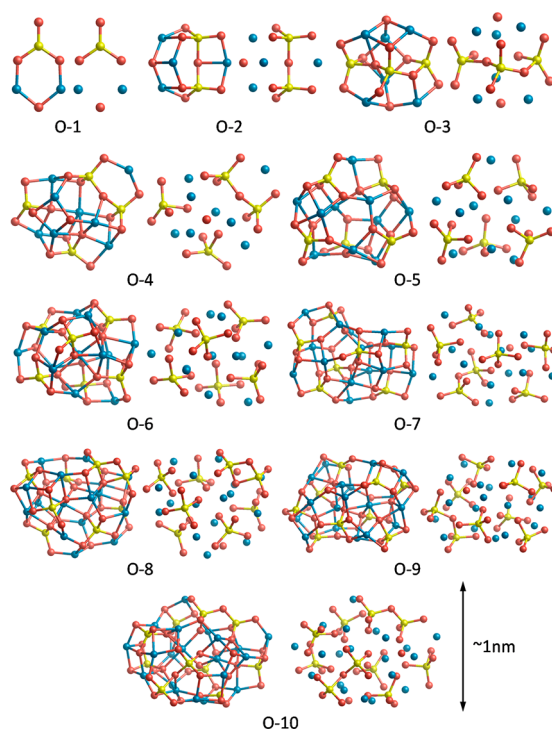

Figure 2. Structures of our GM candidate Mg-rich olivine $(Mg_2SiO_4)_N$ nanoclusters (O-N) for $N = 1-10$. For each size, we show the bonding connectivity of all atoms (left) and that of only the bonded Si−O skeleton (right). Atom key: Si, yellow; O, red; and Mg, blue.

O-3 nanocluster is also close to having a structure with C_s symmetry that is broken by small distortions. For pyroxene nanoclusters, P-1, P-2, and P-6 have structures with C_{2v}, C_{2h}, and C_i point group symmetries, respectively. A more symmetric C_{2h} version of the P-6 $(MgSiO_3)_6$ structure is also found in a very low energy $(Al_2O_3)_6$ nanocluster isomer.[43] Attempts to optimize our candidate GM $(MgSiO_3)_6$ P-6 structure in this higher symmetry spontaneously relaxed to the more stable C_i structure probably because of the symmetry-breaking influence of the two cation types. The P-3 and P-4 nanoclusters can also be viewed as having structures in which energy-lowering distortions have broken a higher C_{2v} symmetry to form a C_1 structure. We note that the P-4 and O-3 nanoclusters were employed in a previous study modeling the formation and dissociation of H_2 on nanosilicate dust grains.[44,45] The P-4 nanocluster was also used in a study of absorption of water on nanosilicates.[65] All other nanocluster structures are reported herein for the first time.

[SiO_4]^{4−} Polymerization. In the olivine Mg_2SiO_4 composition, two Mg^{2+} cations formally balance the charge of each $[SiO_4]^{4−}$ anion. Indeed, the structure of bulk crystalline forsterite can be viewed as an interacting ordered array of such discrete ionic species. However, if $[SiO_4]^{4−}$ tetrahedra begin to segregate and share oxygen atoms (i.e., $[SiO_3−O−SiO_3]^{6−}$), then this in turn frees up $O^{2−}$ ions that then can coordinate with Mg^{2+} cations to promote MgO-rich regions (i.e., MgO segregation). Generally, a low degree of ≡Si−O−Si≡ polymerization implies less segregation and vice versa. In bulk systems with the Mg_2SiO_4 composition, such segregation appears to be strongly energetically disfavored and the dimerization of $[SiO_4]^{4−}$ tetrahedra is typically observed only in high pressure phases (e.g., wadsleyite). Consistent with the
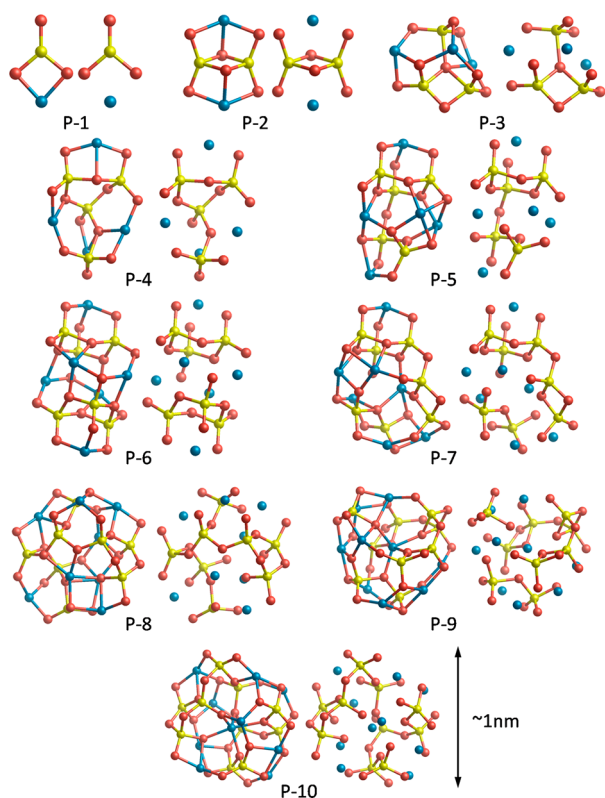
Figure 3. Structures of our GM candidate Mg-rich pyroxene $(MgSiO_3)_N$ nanoclusters (P-N) for $N = 1-10$. For each size, we show the bonding connectivity of all atoms (left) and that of only the bonded Si−O skeleton (right). Atom key: Si, yellow; O, red; and Mg, blue.

structure of low-energy bulk Mg_2SiO_4 crystalline phases under ambient conditions, our candidate GM olivine nanocluster structures have a much lower degree of polymerization than do previously reported nanoclusters.[40,41] With increasing system size, the most energetically stable nanoclusters should approach their respective bulk limit in terms of properties and structure. The size-dependent evolution of oxide nanocluster properties toward the bulk is very system-specific and is typically highly nonmonotonic at small system sizes.[46] However, on average we expect that the degree of polymerization (i.e., number and size of polymers) in our olivine nanoclusters should diminish with increasing size. The smallest olivine nanoclusters, O-2 and O-3, are found to be fully polymerized and exhibit segregated structures containing a $[Si_2O_7]^{6-}$ dimer and a $[Si_3O_{10}]^{8-}$ trimer for O-3. For O-4, half of the four $[SiO_4]^{4-}$ tetrahedra are dimerized, with the other two being isolated. O-5 and O-6 both contain no polymers and are fully mixed systems with all $[SiO_4]^{4-}$ tetrahedra isolated. Surprisingly, a small degree of polymerization appears again for O-7 whereby two of the $[SiO_4]^{4-}$ tetrahedra (<30%) are dimerized. Our best GM candidate for O-8 also exhibits a single dimer, but in this case, two $[SiO_4]^{4-}$ units share two oxygen atoms to form a Si_2O_2 ring. Such strained "two-rings" are not typically found in stable bulk silicates but are known to be high-energy local reconstructions on the surfaces of amorphous pure silica.[47] Two-rings are, however, commonly found in small low energy nanoclusters of pure silica.[20] In the case of O-8, the Si_2O_2 two-ring resides on the surface of the nanocluster, but it is not clear why this particular structure is more stable than many others in our searches that do not

display such a ring. The O-9 nanocluster possesses a single oxygen-bridged dimer, meaning that ~22% of the $[SiO_4]^{4-}$ tetrahedra are polymerized. The O-10 structure possesses two such dimers with six isolated $[SiO_4]^{4-}$ units. Although the trends in the number and length of polymers in our $(Mg_2SiO_4)_N$ GM candidates are not simply monotonically decreasing with increasing N, we note that (i) the highest degree of polymerization (i.e., 100%) is found for O-2 and O-3, (ii) polymerization is mainly limited to dimerization, with only one instance of a trimer polymer in O-3, and (iii) the number of nonpolymerized isolated $[SiO_4]^{4-}$ units tends to increase with size (e.g., 0−2 for O-1−O-4 and 5−7 for O-5−O-10).

Because of the higher Si/O ratio in pyroxene (1:3) relative to that in olivine (1:4), a correspondingly higher degree of polymerization (i.e., oxygen sharing) in pyroxene is necessary to maintain the four-coordination of the $[SiO_4]^{4-}$ units. In the bulk crystalline $MgSiO_3$ enstatite phase, this is achieved through the formation of linear polymers chains in which every $[SiO_4]^{4-}$ tetrahedral unit participates in two single-oxygen bridges with two other units. Similarly, in finite $(MgSiO_3)_N$ nanoclusters a relatively higher degree of polymerization is necessary relative to olivine nanoclusters. In our candidate GM pyroxene nanoclusters, polymerization occurs via the formation of closed rings and/or branched networks. For the very small P-2 and P-3 nanoclusters, the polymerization needed to ensure four-coordination of the $[SiO_4]^{4-}$ units results in the formation of two-rings and/or triply shared oxygen centers. Nanoclusters P-4 and P-5 have more extended branched polymeric networks which exhibit a single $(SiO)_3$ three-ring. P-6 can be seen as a simple structural extension of P-5, which results in a symmetric nanocluster structure with two nonlinked three-rings. Similarly, P-7 can be viewed as an extension of P-6 in which the symmetry is lost and the two distinct three-rings become a dimer and a branched network containing a three-ring and a two-ring, respectively. Nanoclusters P-8 and P-10 contain branched networks containing one three-ring. The P-9 structure is unusual because it contains three silicate groups, one nonpolymerized isolated $[SiO_4]^{4-}$ tetrahedron, a $[Si_2O_7]^{-6}$ dimer, and a six-membered chain which contains three two-rings. Although all of these pyroxene nanoclusters are relatively highly polymerized, often with a single network of $[SiO_4]^{4-}$ tetrahedra, there does not appear to be any simple tendency with respect to the type/degree of polymerization in nanoclusters over the considered size range.

$[SiO_4]^{4-}$ Tetrahedral Distortion. For both the P-N and O-N nanoclusters, the overall structural distortion of the $[SiO_4]^{4-}$ tetrahedral units, with respect to perfect tetrahedrality, decreases with increasing N. Specifically, in Figure 4 we show how the root-mean-square (rms) O−Si−O angle over all $[SiO_4]^{4-}$ units in each nanocluster relative to the symmetric unstrained angle of 109.47° (i.e., $\Delta_{O-Si-O} = \langle abs(\theta_{O-Si-O} - 109.47)\rangle$) varies with N, as compared with the bulk values of enstatite (4.4°) and forsterite (6.5°). Generally, the overall trend is for Δ_{O-Si-O} values to decrease with increasing N, indicating a corresponding decrease in internal structural strain with increasing nanocluster size. However, the two classes of nanoclusters show differences in their structural evolution with size. For small nanocluster sizes ($N < 4$), the pyroxene nanoclusters have notably more tetrahedral distortion than olivine nanoclusters. However, for the P-N nanoclusters the Δ_{O-Si-O} values also rapidly decrease with increasing size, and for $N = 4$, the tetrahedral distortion is lower than in the O-4
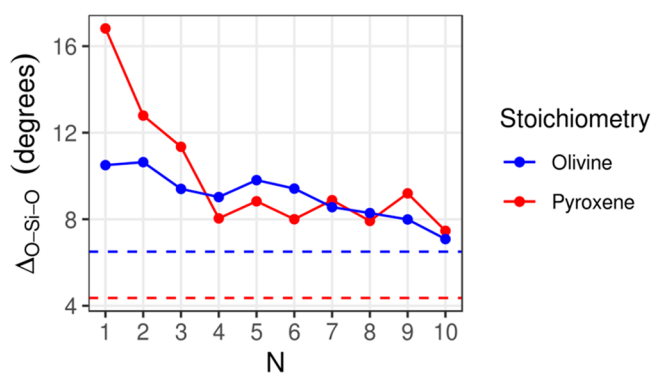
Figure 4. Average tetrahedral distortion of $[SiO_4]^{4-}$ centers ($\Delta_{Si-O-Si}$) with respect to nanocluster size (N) for both the O-N (blue) and P-N (red) series. Dashed lines correspond to the bulk limits of forsterite (blue, 6.5°) and enstatite (red, 4.4°).

nanocluster. For sizes $N \geq 4$, the tetrahedral distortion in the P-N nanoclusters appears to stabilize and exhibits an odd–even oscillation around a value of approximately 8.3°. This result suggests that pyroxene nanoclusters are structurally still far away from the bulk crystalline limit. This can be rationalized by the fact that the inherent spatial confinement of the finite nanoclusters causes the short polymerized $[SiO_4]^{4-}$ chain to be bent and dendritic, unlike the long linear chains in the bulk structure. For O-N nanoclusters with $N \geq 4$, the Δ_{O-Si-O} values tend to keep gradually decreasing with increasing N, and for O-10, they come very close to the bulk limit. This result is in line with the fact that the larger O-N clusters exhibit isolated $[SiO_4]^{4-}$ units as in the bulk forsterite structure.

Mg²⁺ Coordination Number. Silicate polymerization is only one descriptor of the chemical structure of nanosilicates. By examining the changes in the number of bonded neighbors to each Mg^{2+} cation (i.e., the coordination number, CN) throughout the O-N and P-N series, we obtain a complementary perspective on the size-dependent evolution of nanosilicate structure (Figure 5). Generally, for both P-N
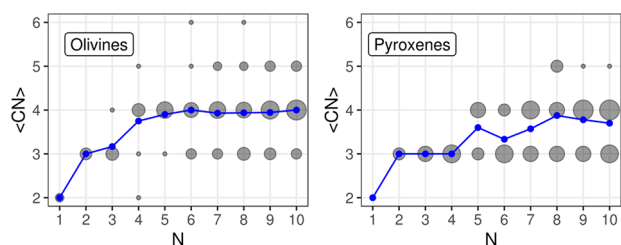

Figure 5. Average coordination numbers of Mg^{2+} cations (i.e., $\langle CN \rangle$) in O-N (left) and P-N (right) nanoclusters (blue lines). The size of the gray disks corresponds to the number of Mg^{2+} cations with a particular coordination in a nanocluster of a given size. A 2.3 Å Mg–O bond cutoff was applied to calculate the coordination values.

and O-N structures the average CN, $\langle CN \rangle$, of Mg^{2+} cations tends to increase with increasing nanocluster size. For the O-N nanoclusters, $\langle CN \rangle$ monotonically increases from 2 (O-1) to 4 (O-6), where it then seems to stabilize for O-7 to O-10 (Figure 5, left). For the P-N nanocluster series, $\langle CN \rangle$ increases in a more irregular fashion from 2 (P-1) to 3.88 (P-8), where it then remains between 3.8 and 3.9 until P-10. We note, in particular, that the $\langle CN \rangle$ value for P-5 appears to be rather high relative to its size, leading to a small peak in the $\langle CN \rangle$

versus size plot in Figure 5 (right). As we will see below, this property is likely related to the anomalous high energy stability of the P-5 nanocluster.

In both sets of nanoclusters, $\langle CN \rangle$ is still always below the typical bulk value of 6 as found in both forsterite and enstatite bulk crystals. This is unsurprising because many of the Mg^{2+} cations in finite nanoclusters are near the surface and have correspondingly fewer oxygen neighbors than within an extended bulk system. Examining individual contributions to $\langle CN \rangle$, we can see that there is indeed a heterogeneous mix of CN values for each Mg^{2+} cation within each nanocluster (gray disks in Figure 5). For the P-N series, the lower and upper bounds of the set of exhibited individual CN values {A, B, etc.} follow a monotonically increasing tendency with increasing nanocluster size: P-1, {2}; P-2–P-4, {3}; P-5–P-7, {3, 4}; P-8–P-10, {3, 4, 5}. See Figure 5 (right). Here, a maximum individual CN value of 5 is achieved, clearly confirming the nonbulk chemical environment of all Mg^{2+} cations in all P-N nanoclusters. For the O-N series, the distribution of CN values for individual Mg^{2+} cations in each nanocluster evolves with size in a more complex fashion. For example, O-4 has a broader set of CN values (i.e., {2, 3, 4, 5}) than do O-3 and O-5 (i.e., {3, 4}), with all three nanoclusters having fairly similar $\langle CN \rangle$ values between 3 and 4. This suggests that O-N nanoclusters can use multiple low-energy structural arrangements of Mg^{2+} cations to compensate for the charge of their $[SiO_4]^{4-}$ anions. This apparent structural freedom is further confirmed by examining the Mg^{2+} CN distributions and overall structures for the largest olivine nanoclusters, O-6–O-10. As in most of the O-N series considered, in these nanoclusters most of the Mg^{2+} cations are four-coordinated. For O-6, unlike for smaller olivine nanoclusters, one finds a centrally located Mg^{2+} cation which allows it to be the first six-coordinated Mg^{2+} in the O-N series. The structures of O-7 and O-8 further exhibit two Mg^{2+} cations linked by two oxygen anions, near their centers. For O-7, both central Mg^{2+} cations are five-coordinated, whereas for the larger O-8 structure one of the central cations is able to attain six-coordination. Although the emergence of six-coordinate Mg^{2+} cations in O-6 and O-8 suggests that the larger O-N nanoclusters are becoming more bulklike, these nanoclusters are still far from having fully bulklike structures. In O-9 and O-10, for example, we see structures that maintain a relatively high $\langle CN \rangle$ by having fewer three-coordinate Mg^{2+} cations and more with Mg^{2+} cations with five-coordination, but display no six-coordinated centers.

Atomically Partitioned Charges. In mineralogy, the atomic structure of silicates is often described and classified in terms of the ordering and polymerization of silicate anionic species with respect to an arrangement of charge-compensating Mg cations (see above). Although silicates are generally ionic insulators, the degree of charge transfer between anions and cations largely depends on the local environment of the ions in question. In crystalline bulk silicates, the periodic space group symmetry dictates that only a limited number of distinct environments for the ions are possible. However, for our silicate nanoclusters, often possessing no point group symmetry, every ion can have a different coordination environment (Figure 5), thus potentially yielding a different ionic charge.

In Figure 6, we plot the Hirshfeld partitioned charges[48] of oxygen anions and magnesium cations with respect to nanocluster size and distance to the center of mass of each nanocluster for both the O-N and P-N series. We note that
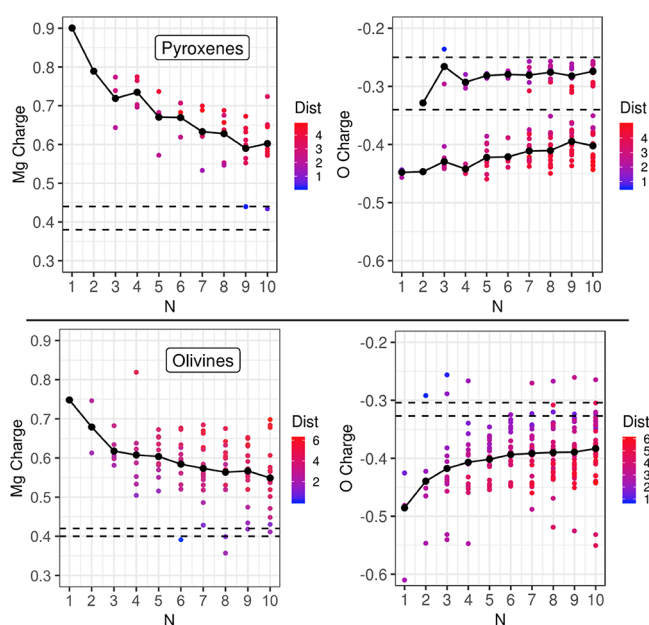
Figure 6. Hirshfeld partitioned charges of Mg cations (left) and O anions (right) in P-N (upper) and O-N (lower) nanoclusters. Dashed lines correspond to bulk crystalline limiting values (i.e., forsterite for the O-N series and enstatite for the P-N series), and black data points and the associated black line follow the corresponding average partitioned charge values with respect to size N. The colors of other data points indicate the distance (in angstroms) between the charged ion and the center of mass of the respective nanocluster according to the respective legend next to each plot.

these partitioned charges are significantly smaller in magnitude than the formal charge states of the constituent ions and do not reflect any observable quantity. Instead, these partitioned charges should be viewed as a consistent means by which to compare the charge distribution in the nanoclusters with respect to variations in size, structure, and composition.

For the O-N nanocluster series, the average partitioned positive Mg charge and the average partitioned negative O charge both decrease in magnitude with increasing nanocluster size. In the bulk olivinic limit of forsterite, Mg cations occupy two crystallographically similar but distinct sites. Atomic charge partitioning reveals these two types of sites to have very slightly different positive charges. The respective bulk limiting values (i.e., for forsterite for the O-N series and for enstatite for the P-N series) are indicated by dashed lines in Figure 6. A corresponding situation is found for O anions which are found to possess slightly different negative partitioned charges. In both cases, the respective average partitioned charges in the O-N clusters are always higher in magnitude than that in the bulk but approach the bulk partitioned charge values with increasing nanocluster size.

In the bulk enstatite crystal, there are two crystallographically distinct oxygen anions with significantly different chemical environments: (i) bridging siloxane oxygen centers (Si−O−Si) and (ii) oxygen centers bonded to a single silicon cation. The former oxygen center is found to have a lower partitioned charge (−0.25 e) than the latter (−0.34 e). Both types of oxygen can be identified in the P-N nanoclusters, and as in the bulk, the siloxane bridging oxygen anions are consistently less negative than the remaining oxygen centers on average. As in the O-N case, the nanocluster-averaged partitioned charges of these oxygen centers are more negative

than their respective bulk counterparts and become progressively less negative with increasing N. The nanocluster-averaged partitioned Mg cationic charges in the P-N series also follow the general trend found for the O-N nanoclusters, whereby the charge magnitude decreases with increasing nanocluster size toward the bulk limits for partitioned Mg cationic charges in forsterite. We note that unlike the Mg and O partitioned charges, the average partitioned silicon charge for all O-N nanoclusters remains unchanged at +0.42 e with a standard deviation of 0.02 and a bulk value of +0.46 e. For P-N nanoclusters, the average partitioned Si charge is +0.46 e with a standard deviation of 0.03, while for enstatite the value is +0.51 e.

In each plot in Figure 6, we color code each individual O and Mg partitioned charge to indicate its distance from the center of mass of the respective nanocluster. First, this analysis shows that the average partitioned charge values for O anions and Mg cations result from a wide range of charge values which, in some cases, can be lower in magnitude than the corresponding bulk charge values. Such an extreme variation reflects the high structural variety in nanoclusters with respect to the ordered crystalline bulk phases. Second, we observe a tendency for partitioned charges to be smaller in magnitude the closer they are to the center of their respective nanocluster. In the plots in Figure 6 we can see this by an increasing blueness (i.e. toward smaller distances) of the data points closer to the bulk limiting dashed lines. This can be rationalized by noting that atoms in the interior of a nanocluster (i.e., nonsurface) have a chemical environment closer to the bulk, and hence they have correspondingly more bulklike charge. With increasing size, the proportion of interior atoms increases; therefore, the average partitioned charge within a nanocluster for each species comes progressively closer to the bulk limit.

Relative Energies. We employ the normalized relative energy, $E_{rel}(N)$ (eq 1) and first-order and second-order energy differences, $\Delta^1(N)$ and $\Delta^2(N)$ (eqs 2 and 3, respectively) to characterize the relative energetic stability of our O-N and P-N nanosilicate clusters:

$$E_{rel}(N) = \frac{E_N}{N} - E_{bulk} \tag{1}$$

$$\Delta^1(N) = E_N - E_{N-1} - E_1 \tag{2}$$

$$\Delta^2(N) = E_N - \frac{E_{N-1} + E_{N+1}}{2} \tag{3}$$

Here, E_N is the total energy of a nanocluster containing N stoichiometric units, and E_{bulk} is the energy per stoichiometric unit of the respective bulk crystalline structure.

In Figure 7, we plot the normalized relative energies for both the O-N and P-N nanocluster series. In both cases, $E_{rel}(N)$ decreases monotonically from $N = 1−10$ with increasing size. From a structural point of view olivine nanoclusters seem to be closer than the pyroxene nanoclusters to the most stable bulk phase. However, the largest O-10 nanocluster is 3.55 eV higher in energy per unit than bulk forsterite, whereas for the same number of units pyroxene is 2.56 eV higher in energy than the enstatite bulk. To provide a rough estimate of the size at which the nanosilicates become bulklike, we fit the $E_{rel}(N)$ data with a third-order polynomial in powers of $N^{-1/3}$ (ref 49):

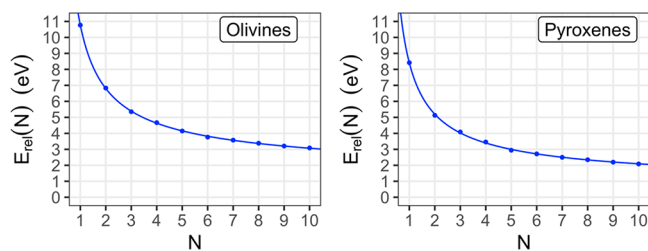$$E_{rel}(N) = a_1 N^{-1/3} + a_2 N^{-2/3} + a_3 N^{-1} \tag{4}$$

G

Figure 7. Energy per stoichiometric unit, $E_{rel}(N)$, for the O-N nanoclusters with respect to forsterite (left) and the P-N nanoclusters with respect to enstatite (right). Blue data points indicate the calculated data, and the blue lines show fits to the data following eq 4.

The resulting fitting lines based on the O-N and P-N total energy data are shown in Figure 7. (All fitting parameters are provided in Table S2 of the SI.) Considering, generally, that metastable bulk polymorphs typically lie, at most, within a few tenths of an eV per unit of the most stable bulk phase, we assume that nanoclusters would become bulklike when $E_{rel}(N) - E_{bulk} < \delta$, where we take δ to be 0.1 eV per atom. For olivine, this criterion provides us with an approximate size of $N = 860$ (i.e., 6020 atoms), whereas for pyroxene we obtain a smaller size of $N = 380$ (i.e., 1900 atoms). Although these are relatively crude assessments, it suggests that at least a few thousand atoms are required for nanosilicates to start to exhibit bulklike energy stabilities. Interestingly, these estimates also suggest that pyroxene attains a more bulklike energetic stability at smaller sizes than olivine.

In Figure 8, we plot the first-order energy difference, $\Delta^1(N)$, and the second-order energy difference, $\Delta^2(N)$, for both the
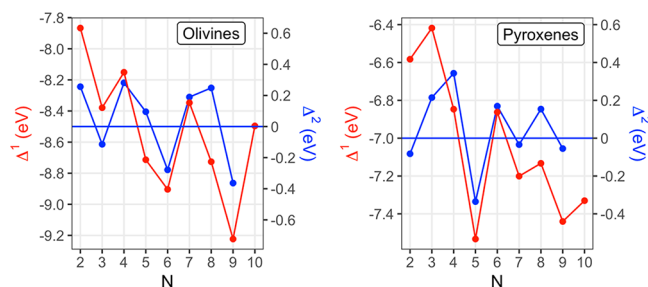

Figure 8. First-order (red line, left vertical axes) and second-order (blue line, right vertical axes) energy differences for the O-N (left) and P-N (right) nanoclusters.

O-N and P-N nanoclusters with respect to nanocluster size. The first-order energy difference provides a measure of stability for a nanocluster with N units with respect to a nanocluster of $N - 1$ units and the $N = 1$ monomer. In this sense, $\Delta^1(N)$ can be thought of as a nucleation energy where more negative values indicate an energetically favored incremental $N - 1 \rightarrow N$ size increase and positive values indicate the converse. The second-order energy difference measures the energy stability of a nanocluster with N units with respect to nanoclusters with both $N - 1$ and $N + 1$ units. For both measures, the appearance of pronounced dips for specific values of N confirms the particularly high relative stability of this nanocluster size with respect to neighboring nanocluster sizes. Values of N with high relative stability as shown by $\Delta^1(N)$ and $\Delta^2(N)$ are referred to as magic numbers. Magic number nanoclusters are found in many systems and are usually found to have relatively high abundances in the

distribution of nanocluster sizes in cluster beam experiments.[50] For olivine, the O-3, O-6, and O-9 sequences of nanoclusters exhibit pronounced dips for $\Delta^2(N)$ and, to a lesser extent, for $\Delta^1(N)$. These nanoclusters do not appear to have any common structural features and have no symmetry. Of these three nanoclusters, O-9 has the lowest values for both measures and this is the most magic size for the olivine series. For the pyroxene nanoclusters, although P-7 and P-9 show dips for $\Delta^1(N)$ and $\Delta^2(N)$, the clearest signal of magic number stability is for P-5, which has very pronounced dips for both measures. Although the P-5 nanocluster has no symmetry, its high relative stability may be linked to its relatively high Mg cation coordination for its size (Figure 5).

We note that $\Delta^1(N)$ and $\Delta^2(N)$ are very sensitive measures of the relative energy stability, and it is thus interesting to establish whether the stability trends they predict are also valid at finite temperatures. We note that many dust-containing astrophysical environments (e.g., the ISM) have rather low temperatures (≤ 100 K) and pressures, so the change in our 0 K results will be negligible. However, in circumstellar regions of evolved stars,[6] nanosilicates are thought to start nucleating at temperatures close to 1000 K. One may also consider the standard laboratory conditions to be relatively extreme compared to those of the ISM. In section S3 of the SI, we calculate the $\Delta^1(N)$ and $\Delta^2(N)$ values for our P-N and O-N nanoclusters based on their finite temperature free energies under standard terrestrial conditions (298 K and 101 300 Pa) and circumstellar conditions (1000 K and 0.0005 Pa). From this analysis, we can see that the general tendencies predicted by our energetics calculated at 0 K are maintained for all O-N nanoclusters. For the P-N nanoclusters, we see little difference under standard conditions, but under circumstellar conditions, the changes are more significant. In particular, we note that the P-5 nanocluster loses its magic stability status and P-9 becomes more magic.

Energies of Formation. The enthalpy of formation of a bulk magnesium silicate from the binary oxides (MgO rock salt and SiO_2 quartz) (ΔH_f^{oxides}) can be derived from

$$\Delta H_f^{oxides}[silicate] = \Delta H_f[(MgO)_a(SiO_2)_b] - (a\Delta H_f[MgO] + b\Delta H_f[SiO_2]) \quad (5)$$

where $\Delta H_f[(MgO)_a(SiO_2)_b]$ is the enthalpy of formation of the magnesium silicate in question and $\Delta H_f[MgO]$ and $\Delta H_f[SiO_2]$ are the enthalpies of formation of the oxides, all relative to the elements. For forsterite (Mg_2SiO_4), stoichiometric coefficients $a = 2$ and $b = 1$ are used, whereas for enstatite ($MgSiO_3$), one should employ $a = b = 1$. Using extrapolated 0 K values from the NIST-JANAF tables of experimental thermodynamic data[51] for the three terms on the right-hand side of eq 5, we obtain $\Delta H_f^{oxides}[forsterite] = -0.66$ eV and $\Delta H_f^{oxides}[enstatite] = -0.38$ eV. We note that these values are within 0.01 eV of directly measured values obtained at 970 K.[52] Using the same level of DFT theory as for the nanoclusters, we find $\Delta H_f^{oxides}[forsterite] = -0.77$ eV and $\Delta H_f^{oxides}[enstatite] = -0.42$ eV, which are in quite good agreement with the experimental values, thus confirming the adequacy of our DFT calculations for silicate energetics. Note that in these theoretical values the calculated internal energies are assumed to be a good approximation to the enthalpies (i.e., pV contributions are taken to be negligible). Because of the fact that both of these silicates have distinct stoichiometries, a direct comparison of these two values is not very informative.

For each silicate family considered, we would like to have a method for comparing the formation energies with their respective bulk values which takes into account the finite size of both the nanosilicate and the oxide components. One way to do this is to find appropriately sized low-energy nanoclusters of MgO and SiO_2 which, when brought together, form a system with the same size and stoichiometry as for a particular silicate nanocluster. Formally, we can describe this energy difference (per stoichiometric unit) by

$$\Delta H_{f(reactive)}^{oxides}[nanosilicate] \approx \Delta E_{f(reactive)}^{oxides}[nanosilicate]$$
$$= \frac{E[(Mg_a Si_b O_{a+2b})_N] - (E[(MgO)_{aN}] + E[(SiO_2)_{bN}])}{N} \quad (6)$$

where N is the number of stoichiometric units in the silicate nanocluster and, as in eq 1, we have $a = 2$ and $b = 1$ for the olivine case and $a = b = 1$ for the pyroxene case. Note that in this case we compare the internal energies of a combined system with $(a + 2b)N$ oxygen anions with two smaller systems containing aN and $2bN$ oxygen anions, respectively. In this sense, we refer to these energies as reactive formation energies (RFEs).

Although nanocluster RFEs can be difficult to obtain experimentally, they can be easily evaluated using the calculated energies of our candidate GM nanosilicates and the corresponding GM nanoclusters for $(MgO)_N$[53,54] and $(SiO_2)_N$.[20] In Figure 9, we plot the RFEs of the P-N and O-N
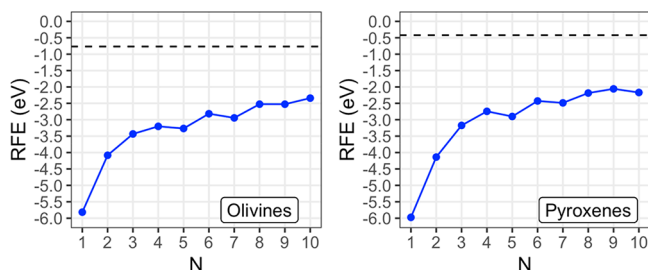

Figure 9. Reactive formation energies (RFEs) for the O-N (left) and P-N (right) silicate nanoclusters with respect to the number of stoichiometric units. In each case, the calculated limiting value of the calculated enthalpy of formation of the respective bulk crystalline silicate is indicated by a dashed line (i.e., forsterite, left; enstatite, right).

nanoclusters (blue lines) with respect to the number of units in each nanocluster. In both cases, the RFE is initially relatively negative because of the high energy stabilization gained from the addition of the smallest and least stable monomeric pure oxide species. With increasing nanocluster size, the internal energies per unit of nanosilicates and the respective pure oxide nanoclusters tend to increasingly stabilize toward the corresponding bulk values. Note that, unlike the simple normalization used to obtain the energy per unit (Figure 7) for the nanoclusters, the RFE energies are dependent on the stabilities of different smaller subclusters for each nanocluster size and thus show some size-dependent fluctuations. However, with increasing size these fluctuations will subside and the RFE values for the P-N series and the O-N nanocluster series will become progressively closer to the calculated bulk enthalpies of formation for enstatite and forsterite, respectively (dashed horizontal lines in Figure 9). Taking the largest O-10 and P-10 nanoclusters, we note that their RFE values are both

still >1.5 eV more negative than the respective bulk ΔH_f^{oxides} values.

An alternative way to calculate silicate nanocluster formation energies is with respect to the proportions of pure oxide nanoclusters which contain the same number of oxygen anions as in the silicate nanocluster in question. In such a formulation, silicate nanoclusters are compared with oxide nanoclusters of a similar size, thus mirroring the calculation of ΔH_f^{oxides} for bulk silicates. The equation for calculating such a "mixing" formation energy (MFE) for nanosilicates is given in eq 7.

$$\Delta H_{f(mixing)}^{oxides}[nanosilicate] \approx \Delta E_{f(size\text{-}consistent)}^{oxides}[nanosilicate]$$
$$= \frac{E(Mg_a Si_b O_{a+2b})_N - \left(\frac{a}{a+2b}E[(MgO)_{(a+2b)N}] + \frac{2b}{a+2b}E[(SiO_2)_{(\frac{a}{2}+b)N}] \right)}{(a+2b)N}$$
$$(7)$$

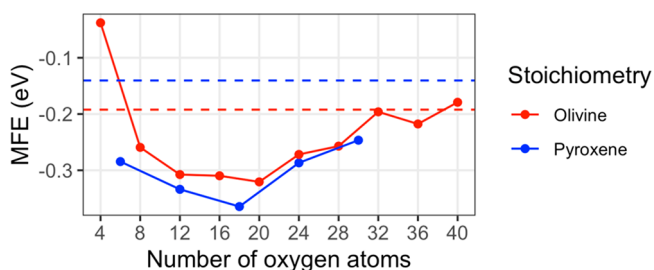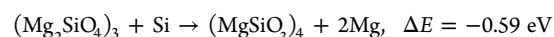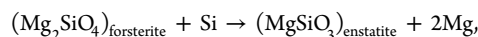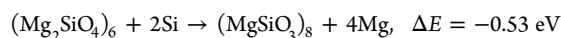The results of the MFE are shown for both pyroxene and olivine systems in Figure 10. As for the RFE values, the MFE

Figure 10. Mixing formation energies (MFEs) of the O-N (red) and P-N (blue) silicate nanoclusters with respect to oxygen content. The dashed lines indicate the calculated bulk enthalpy of formation for forsterite (red) and enstatite (blue) per oxygen atom.

equation implies that with increasing size the MFE will approach the respective enthalpy of formation (per oxygen) of the corresponding bulk. The MFE compares the energy of any particular silicate nanocluster with that of a proportional mix of pure oxide nanoclusters possessing the same number of oxygen cations. As such, the MFE values are not dominated by the energy liberated in a reaction of smaller pure oxide nanoclusters and, unlike the RFE values, do not simply tend to increase monotonically with increasing silicate nanocluster size. Instead, starting from the smallest considered nanoclusters, the MFE values for both pyroxene and olivine nanoclusters initially decrease with increasing size. For nanosilicates with more than approximately 18 oxygen cations, the MFE values in both cases tend to then increase toward their respective bulk limits. Curiously, although the bulk enthalpy of formation per oxygen atom (and thus the bulk MFE) is more negative for forsterite than for enstatite, for the range of oxygen content considered for the nanosilicates the MFE values are more negative for pyroxene than for olivine. This inversion of the MFE values for small sizes has implications for the relative stabilities of nanosilicates. For example, if we take two silicate nanoclusters with the same oxygen content in this inverted MFE regime, we can calculate the total energies of the following Si/Mg exchange reactions and compare with the corresponding bulk case (in square brackets we also include the bulk reaction energy calculated from data in the JANAF tables[51]):

$$(Mg_2SiO_4)_3 + Si \rightarrow (MgSiO_3)_4 + 2Mg, \quad \Delta E = -0.59 \text{ eV}$$

$$(Mg_2SiO_4)_6 + 2Si \rightarrow (MgSiO_3)_8 + 4Mg, \quad \Delta E = -0.53 \text{ eV}$$

$$(Mg_2SiO_4)_{forsterite} + Si \rightarrow (MgSiO_3)_{enstatite} + 2Mg,$$

$$\Delta E = +1.11[+1.84 \text{ eV}]$$

These reactions imply that under nonoxidizing conditions (i.e., limited availability of oxygen), it is energetically favorable to convert olivine nanoclusters to pyroxene nanoclusters via the replacement of Mg by Si, while the analogous bulk process is not energetically viable. In astrophysical environments, atomic Si is often depleted into silicate dust and/or SiO molecules, tending to reduce its availability for such processes. At low-enough temperatures, the latter can condense into $(SiO)_N$ nanoclusters[55] which tend to segregate into O-rich (i.e., silica-like) and Si-rich (i.e., silicon-like) subclusters.[23] Because Si−Si bonds are much weaker than Si−O bonds, dust processing in the ISM (e.g., shocks, sputtering) could potentially then lead to the release of Si from the Si-rich parts of such nanograins. We further note that careful estimates of observed Si depletions in various regions of the ISM have recently been incorporated into dust evolution models. This modeling leads to predictions of the sufficient availability of atomic Si for high silicate dust formation rates, especially in a cold neutral medium.[56] Our mechanism provides one possible route whereby such available Si could then be (re)depleted onto olivinic nanograins, leading to the sputtering of Mg to produce pyroxenic species. In particular, the nanoscale thermodynamic preference for pyroxene could provide an additional route for the observed presence of pyroxene dust,[57,58] where bulk thermodynamics would suggest the favored formation of olivine.[59]

IR Vibrational Spectra. Typical IR spectra from amorphous astronomical silicates have two broad peaks centered around 10 μm and 18−20 μm.[4,60] The more intense 10 μm peak is associated with Si−O stretching modes, and the weaker, longer-wavelength peak is linked to O−Si−O bending modes. Like all silicate grains, nanosilicates will absorb infrared (IR) radiation, and because of their ultrasmall size, they are also subject to single-photon heating and thus are likely to produce well-defined IR emission signatures.[60] Under the assumption that the IR wavelengths at which nanosilicates absorb/emit are the same as those typically associated with bulk laboratory silicates, observational spectra can place some limitations on the potential abundance of nanosilicate species. Assuming a single-sized population of spherical grains, for example, the IR emission intensity with respect to wavelength can thus be estimated for different ultrasmall grain sizes. In this way, without violating any observational IR emission constraints, it has been proposed that up to 15% of the silicon in the diffuse ISM could reside in amorphous nanosilicate grains having diameters ≤1 nm.[9] Such approaches to estimate the IR spectra of nanosilicates are based on approximate top-down methods in that they employ simple geometric representations of grain shapes without atomic detail and dielectric responses derived from those of bulk silicates. Our DFT-based calculations allow us to directly and accurately calculate the oscillatory atomic motions associated with IR-active vibrational modes in our atomistically detailed silicate structures. Herein, we use such an approach to calculate the IR vibrational spectra for our O-N and P-N nanoclusters which all lie in the ≤1-nm-diameter size regime.

A study comparing various functionals for DFT-based calculations of the bulk forsterite crystal using a 28-atom unit cell showed PBE0 to be particularly accurate for capturing silicate atomic structure (differences with respect to experimental parameters are typically <1%) and also for accurately reproducing relative experimental IR oscillator strengths.[61] Reference 62 also showed that the DFT-calculated vibrational frequencies of bulk forsterite using PBE0 were consistently slightly overestimated with respect to experimentally measured values (by 12.3 cm^{-1} on average). To compare our DFT-calculated results more easily with published IR spectra of silicate dust from astronomical observations, we convert the frequencies directly obtained from our calculations to wavelengths in micrometers and add a small amount of Gaussian broadening. We note that an average corrective frequency downshift of 12.3 cm^{-1} would correspond to small corrective wavelength upshifts of only ∼0.1 μm for features close to 10 μm and ∼0.3 μm for features close to 20 μm. In Figures 11 and
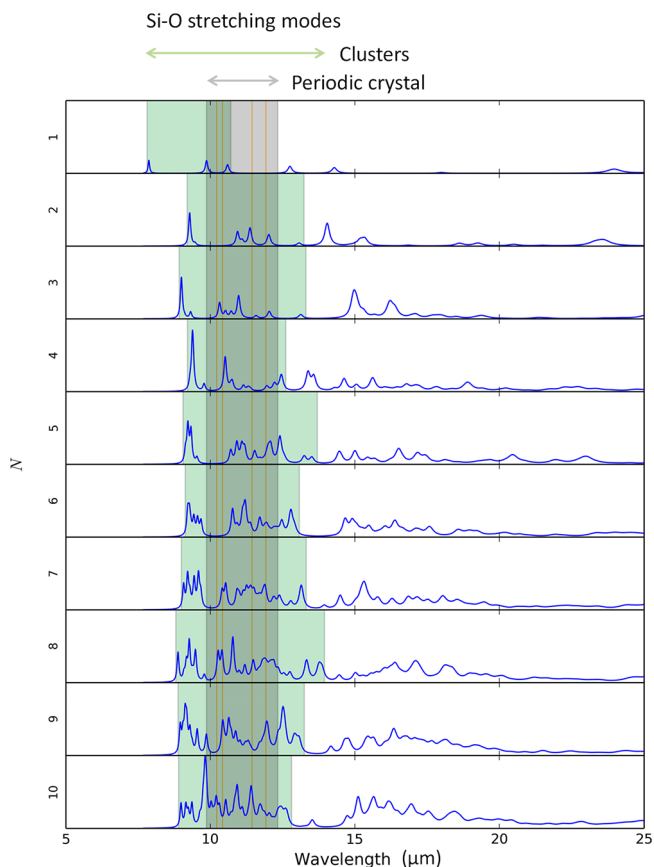

Figure 11. Calculated harmonic IR spectra for the O-N nanoclusters with respect to wavelength (blue line). The gray shaded region spans the wavelength range corresponding to Si−O stretching modes calculated for the bulk forsterite crystal (where vertical orange lines correspond to experimental peak positions of the IR reflection spectra[62]). The green shaded regions show the corresponding wavelength range where Si−O stretching modes can be identified for each nanocluster (note that O−Si−O bending modes can also be found in these regions). The overlap of green and gray regions is indicated by dark-green shading.

12, we show the uncorrected DFT-calculated IR spectra for the O-N and P-N nanoclusters, respectively. In these figures, we highlight the wavelength range associated with Si−O stretching modes for the respective bulk crystal (gray area) and the wavelengths of the corresponding main crystalline bands within this region (red lines). With respect to the calculated spectra of the corresponding crystalline bulk systems, in the
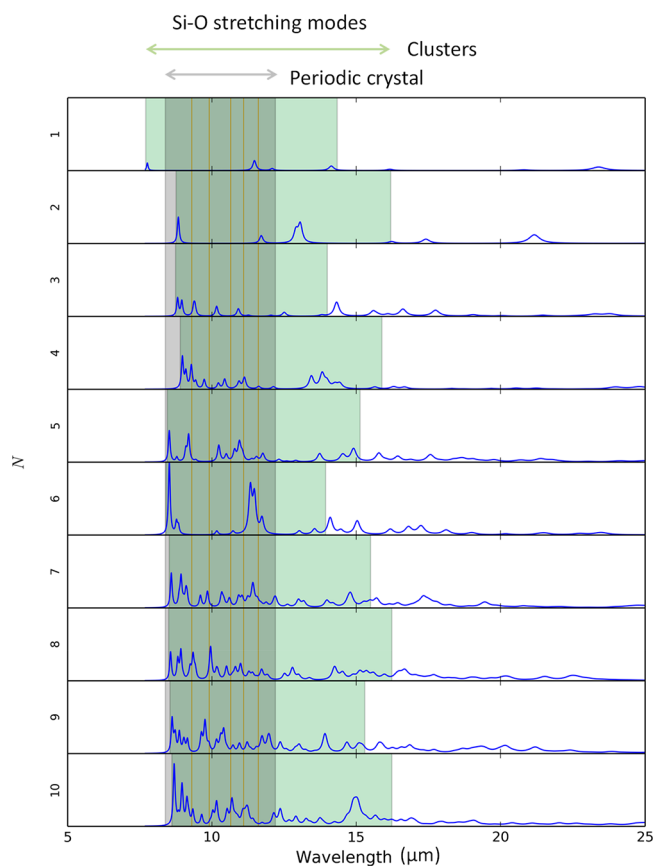
Figure 12. Calculated harmonic IR spectra for P-*N* nanoclusters with respect to wavelength (blue line). The gray shaded region spans the wavelength range corresponding to Si−O stretching modes calculated for the bulk clinoenstatite crystal (where vertical orange lines correspond to experimental peak positions of the mass absorption coefficients[63]). The green shaded regions show the corresponding wavelength range where Si−O stretching modes can be identified for each nanocluster. (Note that O−Si−O bending modes can also be found in these regions.) The overlap of green and gray regions is indicated by dark-green shading.

nanoclusters the lower-wavelength peaks corresponding to Si−O asymmetric stretching tend to cover a broader wavelength range (green shading in Figures 11 and 12). These regions tend to be reasonably symmetrically broadened in the O-*N* nanoclusters with respect to that for forsterite. For the pyroxene nanoclusters, however, the region of Si−O stretching modes starts at a very similar wavelength to that in bulk enstatite but then extends to much longer wavelengths (often to >15 μm as compared to the bulk enstatite upper limit of ~12 μm). Such differences are likely due to the distinct size-induced atomic structure of the nanoclusters (see above) relative to the periodic atomic order found in crystalline bulk systems.

Unlike typical IR spectra from astronomical silicate sources, the calculated IR spectra of the individual nanoclusters clearly have a great deal of discernible detail because of the fact that these small nanoclusters possess a relatively small number of vibrational degrees of freedom. This molecular-like character is clearly more evident in the smaller clusters than in the larger nanosilicates, where individual peaks start to overlap to form broader features. Even for the larger nanosilicate clusters considered, however, there are a number of significant distinct peaks in the 8−12 μm region. It is of note that very few of the

individual nanocluster spectra have significant IR oscillator strengths at or very close to 10 μm (e.g., O-10). As such, it is not clear to what extent silicate nanoclusters would contribute to the observed 10 μm Si−O stretching feature. We also note that, generally, the well-defined peaks in the Si−O stretching regions of the nanocluster spectra do not coincide with those of the corresponding bulk crystal. In those few cases where there is a match between nanocluster and bulk IR Si−O peaks (e.g., for O-8 and P-8), this is clearly not due to a structural correspondence between the two systems and is likely just a coincidence.

For longer wavelengths, none of the pyroxene clusters exhibit significant IR peaks beyond 15−17 μm. For the olivine clusters, some discernible IR peaks can be found at up to 18 to 19 μm. The double-peaked spectra observed for noncrystalline astronomical silicates are best matched by the spectra for O-*N* nanoclusters, especially for $N \geq 6$. For this set of nanoclusters, two main regions of the spectra can be distinguished: (i) a Si−O stretching region between approximately 8 and 14 μm and (ii) a longer-wavelength region between 14 and 21 μm. In the latter region, the more intense peaks tend to be found in the 15−18 μm range and are thus at shorter wavelengths than usually observed for astronomical silicate dust (i.e., 18−20 μm).

We note that our reported spectra correspond only to the lowest-energy GM silicate nanoclusters and do not currently consider contributions from metastable nanosilicate isomers in the size range considered. A comparison of DFT-derived IR spectra with spectra from cluster beam experiments indicates that the contributions from the lowest-energy cluster isomers often dominate the measured spectra.[64] However, in astrophysical environments, various processing phenomena could yield distributions of nanoclusters that are not dominated by thermodynamics and that have contributions from large ensembles of dust particles with diverse structures. To begin to see the effect of mixing spectra from nanosilicate grains with different structures and sizes, in Figure 13 we show
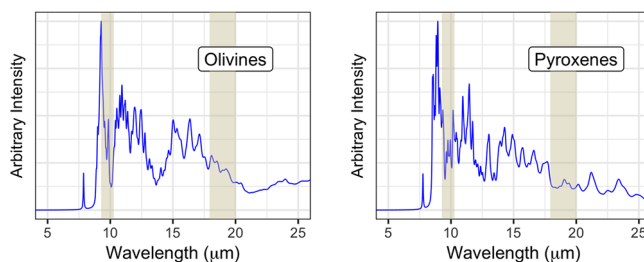

Figure 13. Spectra resulting from equally weighted sums of (i) all spectra from O-*N* nanoclusters in Figure 11 (left) and (ii) all spectra from P-*N* nanoclusters in Figure 12 (right). Shaded bars indicate typical wavelength ranges for the two main features assigned to noncrystalline silicate dust.

the spectra resulting from equally weighted sums of all O-*N* spectra (left) and of all P-*N* spectra (right). In Figure 13, we also highlight wavelength regions typical of astronomical silicate IR spectra with gray areas at 9.7 ± 0.5 μm and at 18−20 μm. Consistent with the above discussion of IR spectra of individual nanoclusters, in both summed spectra in Figure 13 we find that the 18−20 μm region is relatively weak and instead we have greater intensity in the 14−18 μm range. In both spectra we also find two main peaks on either side of 10 μm rather than a single feature peaking at around 10 μm. In

both cases, we also find a sharp feature at around 9.1 μm and a broader set of less intense peaks spanning a wavelength range approximately between 10.2 and 12.5 μm.

The clear difference between our calculated IR nanosilicate spectra and those typically observed and assigned to silicate dust raises some questions. For example, the poor match between our calculated IR spectra and those observed in circumstellar outflows of evolved stars (where the nucleation of nanosilicates is thought to occur) could provide evidence that nucleation predominantly occurs on other seed species rather than on nanosilicates forming directly. Another possibility could be that nanosilicates in such environments are present but are very short-lived species (because of growth into larger grains) and thus their net populations are very small. Generally, our accurate calculated data for silicate nanoclusters in the ≤1-nm-diameter size regime show that the assumption that nanosilicates display IR spectra analogous to those of bulk silicates is not always valid. As such, much care should be taken when assessing the astronomical abundances of nanosilicates based on bulk silicate interpretations of observed IR spectra.[9]

■ CONCLUSIONS

Through the development of an IP that has been specifically tuned for describing the structures and energetics of nanosilicates, we perform extensive global optimization searches to find new candidate GM isomers for olivine $(Mg_2SiO_4)_N$ and pyroxene $(MgSiO_3)_N$ nanoclusters for N = 1−10. Using quantum chemical DFT calculations, we refine our search results to obtain more accurate energies, structures, and properties of our obtained nanosilicates. In particular, we track the evolution of chemical structure, relative energies, energies of formation, ionic charge distributions, and IR spectra with nanocluster size and composition. Whenever possible we compare these results with those from analogous accurate calculations on bulk silicate crystals (i.e., enstatite and forsterite).

Both O-N and P-N nanoclusters tend to have rather irregular structures with only a few exhibiting symmetric or nearly symmetric atomic arrangements. Although there is no indication of crystalline structure, in all cases, some of the larger O-N nanoclusters have all of their $[SiO_4]^{4-}$ units as nonpolymerized isolated species and also begin to exhibit occasional six-coordinate Mg^{2+} cations, as found in the corresponding bulk forsterite crystal. The sizes and structures of our reported nanoclusters are also strongly linked to their ionic charge distributions. We find that the magnitude of the average atomically partitioned charges of the oxygen anions and magnesium cations decreases with increasing size of both O-N and P-N nanoclusters toward their respective bulk values. However, in line with their rather irregular structures there is a large scattering of cationic and anionic charges in all nanoclusters.

Within the set of nanoclusters studied, we find that some have relatively high energy stabilities with respect to other nanoclusters of the same composition and similar size (e.g., O-9 and P-5) and are thus predicted to be magic number clusters at low temperatures. For larger nanoclusters, extrapolating how the energy stability per unit of the O-N and P-N series evolves with increasing size, we roughly estimate that a crossover to bulklike crystalline stability would require having silicate nanoparticles with at least ∼2000 atoms (pyroxene) and ∼6000 atoms (olivine). The energies of formation of our magnesium silicate nanoclusters with respect to the reaction from constituent subclusters of MgO and SiO_2 (i.e., the RFE values) approach the corresponding bulk crystal energies of formation from below in a nearly monotonically increasing fashion. The energies of formation of our silicate nanoclusters were also calculated with respect to a normalized mixture of MgO and SiO_2 nanoclusters, both with the same oxygen content as the silicate nanocluster under consideration, (i.e., the MFE values). With increasing size the silicate nanocluster MFE values should converge to the energy of formation values per oxygen atom of the respective bulk silicate. Unlike for RFE values, the MFE values pass through a minimum (for nanoclusters containing 18−20 oxygen anions) before approaching toward bulk values for larger nanocluster sizes. For sizes near this minimum, the MFE values for pyroxene nanoclusters are lower than those for olivine nanoclusters, which is the inverse of the situation for the bulk energies of formation per oxygen atom for enstatite and forsterite, respectively. This unexpected higher stability for small pyroxene nanoclusters relative to olivine nanoclusters, under conditions when oxygen availability is limited, has potential implications for astrophysical dust processing and/or formation (e.g., circumstellar environments, the ISM, and exoplanetary atmospheres).

Finally, we report the calculated harmonic IR spectra of all considered silicate nanoclusters. As expected from their small size, all spectra have a number of discernible peaks. However, in line with their noncrystalline structures, few of the peaks in the nanosilicate spectra have wavelengths which match those of the IR spectra from bulk silicate crystals. For the Si−O stretching region, the O-N and P-N nanoclusters typically have IR peaks with both longer and shorter wavelengths than those found for forsterite and enstatite, respectively. The O−Si−O bending band of typical IR spectra for astronomical silicates typically covers an 18−20 μm range. In the P-N nanoclusters, we find very little intensity for the O−Si−O bending modes. For the O-N nanoclusters, we find more significant peaks for these modes but with the highest intensity concentrated over a 15−18 μm interval. A sum of spectra for each respective nanosilicate family confirms this general picture and also highlights that the 10 μm Si−O bending feature for our nanosilicates tends to be split into two components above and below 10 μm.

Overall, we provide a systematic bottom-up study of the structure, energetics, and properties of stable Mg-rich nanosilicates with both olivine and pyroxene stoichiometries. Our results, based on accurate electronic structure calculations of atomically detailed nanoclusters, highlight clear differences between nanosilicates and bulk silicates and how the former approaches the latter with increasing size. Our analyses thereby underline the limitations of trying to understand and rationalize the properties of ultrasmall nanosilicate grains by using traditional top-down approaches extrapolating from bulk silicate properties. Overall, we provide a new platform for an accurate and detailed understanding of nanoscale silicates which we hope will be of use in both earth and space sciences.

■ ASSOCIATED CONTENT

Ⓢ Supporting Information

The Supporting Information is available free of charge on the ACS Publications website at DOI: 10.1021/acsearthspacechem.9b00139.

Parameters for the MgFFSiOH IP, parameters used for fitting energy versus size data, IP versus DFT relative energy correlation plots using different IPs for $(Mg_2SiO_4)_6$ and $(MgSiO_3)_7$ isomers, free-energy-corrected $\Delta^1(N)$ and $\Delta^2(N)$ values for all O-N and P-N nanoclusters, and Cartesian coordinates for all O-N and P-N nanoclusters (PDF)

■ AUTHOR INFORMATION

Corresponding Authors
*E-mail: Scott.Woodley@ucl.ac.uk
*E-mail: s.bromley@ub.edu

ORCID ⊙
Tomas Lazaukas: 0000-0002-8351-9857
Scott M. Woodley: 0000-0003-3418-9043
Stefan T. Bromley: 0000-0002-7037-0475

Notes
The authors declare no competing financial interest.

■ REFERENCES

(1) Lutgens, F. K.; Tarbuck, E. J.; Tasa, D. *Essentials of Geology*, 11th ed.; Pearson Prentice Hall, 2012.

(2) Hochella, M. F.; Lower, S. K.; Maurice, P. A.; Penn, R. L.; Sahai, N.; Sparks, D. L.; Twining, B. S. Nanominerals, Mineral Nano-particles, and Earth Systems. *Science (Washington, DC, U. S.)* 2008, 319 (5870), 1631−1635.

(3) Plane, J. M. C. Cosmic Dust in the Earth's Atmosphere. *Chem. Soc. Rev.* 2012, 41 (19), 6507.

(4) Henning, T. Cosmic Silicates. *Annu. Rev. Astron. Astrophys.* 2010, 48 (1), 21−46.

(5) Molster, F. J.; Kemper, C. Crystalline Silicates. *ISO Science Legacy*; Springer-Verlag: Berlin, 2005; Vol. 119, pp 3−28. .

(6) Gail, H.-P.; Sedlmayr, E. *Physics and Chemistry of Circumstellar Dust Shells*; Cambridge University Press: Cambridge, 2013. .

(7) Bringa, E. M.; Kucheyev, S. O.; Loeffler, M. J.; Baragiola, R. A.; Tielens, A. G. G. M.; Dai, Z. R.; Graham, G.; Bajt, S.; Bradley, J. P.; Dukes, C. A.; et al. Energetic Processing of Interstellar Silicate Grains by Cosmic Rays. *Astrophys. J.* 2007, 662 (1), 372−378.

(8) Kemper, F.; Vriend, W. J.; Tielens, A. G. G. M. The Absence of Crystalline Silicates in the Diffuse Interstellar Medium. *Astrophys. J.* 2004, 609 (2), 826−837.

(9) Li, A.; Draine, B. T. On Ultrasmall Silicate Grains in the Diffuse Interstellar Medium. *Astrophys. J.* 2001, 550 (2), L213−L217.

(10) Charnay, B.; Bézard, B.; Baudino, J.-L.; Bonnefoy, M.; Boccaletti, A.; Galicher, R. A Self-Consistent Cloud Model for Brown Dwarfs and Young Giant Exoplanets: Comparison with Photometric and Spectroscopic Observations. *Astrophys. J.* 2018, 854 (2), 172.

(11) Burrows, A.; Sharp, C. M. Chemical Equilibrium Abundances in Brown Dwarf and Extrasolar Giant Planet Atmospheres. *Astrophys. J.* 1999, 512 (2), 843−863.

(12) Jäger, C.; Dorschner, J.; Mutschke, H.; Posch, T.; Henning, T. Steps toward Interstellar Silicate Mineralogy. *Astron. Astrophys.* 2003, 408 (1), 193−204.

(13) Wales, D.; Doye, J. P. K. Global Optimization by Basin-Hopping and the Lowest Energy Structures of Lennard-Jones Clusters Containing up to 110 Atoms. *J. Phys. Chem. A* 1997, 101 (97), 5111−5116.

(14) Lazauskas, T.; Sokol, A. A.; Woodley, S. M. An Efficient Genetic Algorithm for Structure Prediction at the Nanoscale. *Nanoscale* 2017, 9 (11), 3850−3864.

(15) Blum, V.; Gehrke, R.; Hanke, F.; Havu, P.; Havu, V.; Ren, X.; Reuter, K.; Scheffler, M. Ab Initio Molecular Simulations with Numeric Atom-Centered Orbitals. *Comput. Phys. Commun.* 2009, 180 (11), 2175−2196.

(16) Adamo, C.; Barone, V. Toward Reliable Density Functional Methods without Adjustable Parameters: The PBE0 Model. *J. Chem. Phys.* 1999, 110 (13), 6158−6170.

(17) Lamiel-Garcia, O.; Ko, K. C.; Lee, J. Y.; Bromley, S. T.; Illas, F. When Anatase Nanoparticles Become Bulklike: Properties of Realistic TiO_2 Nanoparticles in the 1−6 nm Size Range from All Electron Relativistic Density Functional Theory Based Calculations. *J. Chem. Theory Comput.* 2017, 13 (4), 1785−1793.

(18) Li, Z.; Scheraga, H. A. Monte Carlo-Minimization Approach to the Multiple-Minima Problem in Protein Folding. *Proc. Natl. Acad. Sci. U. S. A.* 1987, 84 (19), 6611−6615.

(19) Bromley, S. T.; Flikkema, E. Columnar-to-Disk Structural Transition in Nanoscale $(SiO_2)_N$ Clusters. *Phys. Rev. Lett.* 2005, 95, 185505.

(20) Flikkema, E.; Bromley, S. T. Dedicated Global Optimization Search for Ground State Silica Nanoclusters: $(SiO_2)_N$ (N = 6−12). *J. Phys. Chem. B* 2004, 108 (28), 9638−9645.

(21) Jelfs, K. E.; Flikkema, E.; Bromley, S. T. Hydroxylation of Silica Nanoclusters $(SiO_2)_M(H_2O)_N$, M = 4, 8, 16, 24: Stability and Structural Trends. *Phys. Chem. Chem. Phys.* 2013, 15 (47), 20438−20443.

(22) Cuko, A.; Calatayud, M.; Bromley, S. T. Stability of Mixed-Oxide Titanosilicates: Dependency on Size and Composition from Nanocluster to Bulk. *Nanoscale* 2018, 10 (2), 832−842.

(23) Bromley, S. T.; Gómez Martín, J. C.; Plane, J. M. C. Under What Conditions Does $(SiO)_N$ Nucleation Occur? A Bottom-up Kinetic Modelling Evaluation. *Phys. Chem. Chem. Phys.* 2016, 18 (38), 26913−26922.

(24) Goumans, T. P. M.; Bromley, S. T. Efficient Nucleation of Stardust Silicates via Heteromolecular Homogeneous Condensation. *Mon. Not. R. Astron. Soc.* 2012, 420 (4), 3344−3349.

(25) Cuko, A.; Maciá, A.; Calatayud, M.; Bromley, S. T. Global Optimisation of Hydroxylated Silica Clusters: A Cascade Monte Carlo Basin Hopping Approach. *Comput. Theor. Chem.* 2017, 1102, 38−43.

(26) Hjorth Larsen, A.; Jørgen Mortensen, J.; Blomqvist, J.; Castelli, I. E.; Christensen, R.; Dułak, M.; Friis, J.; Groves, M. N.; Hammer, B.; Hargus, C.; et al. The Atomic Simulation Environment—a Python Library for Working with Atoms. *J. Phys.: Condens. Matter* 2017, 29 (27), 273002.

(27) Gale, J. D.; Rohl, A. L. The General Utility Lattice Program (GULP). *Mol. Simul.* 2003, 29 (5), 291−341.

(28) Dick, B. G.; Overhauser, a. W., Jr; BG Dick; Overhauser, A. Theory of the Dielectric Constants of Alkali Halide Crystals. *Phys. Rev.* 1958, 112 (1), 90−103.

(29) Woodley, S. M. Knowledge Led Master Code Search for Atomic and Electronic Structures of LaF_3 Nanoclusters on Hybrid

Rigid Ion−Shell Model−DFT Landscapes. *J. Phys. Chem. C* **2013**, *117* (45), 24003−24014.

(30) Mora-Fonz, D.; Lazauskas, T.; Farrow, M. R.; Catlow, C. R. A.; Woodley, S. M.; Sokol, A. A. Why Are Polar Surfaces of ZnO Stable? *Chem. Mater.* **2017**, *29* (12), 5306−5320.

(31) Escher, S. G. E. T.; Lazauskas, T.; Zwijnenburg, M. A.; Woodley, S. M. Structure Prediction of $(BaO)_n$ Nanoclusters for $n \leq$ 24 Using an Evolutionary Algorithm. *Comput. Theor. Chem.* **2017**, *1107*, 74−81.

(32) Lazauskas, T.; Sokol, A. A.; Buckeridge, J.; Catlow, C. R. A.; Escher, S. G. E. T.; Farrow, M. R.; Mora-Fonz, D.; Blum, V. W.; Phaahla, T. M.; Chauke, H. R.; et al. Thermodynamically Accessible Titanium Clusters Ti_N, N = 2−32. *Phys. Chem. Chem. Phys.* **2018**, *20* (20), 13962−13973.

(33) Mora-Fonz, D.; Lazauskas, T.; Woodley, S. M.; Bromley, S. T.; Catlow, C. R. A.; Sokol, A. A. Development of Interatomic Potentials for Supported Nanoparticles: The Cu/ZnO Case. *J. Phys. Chem. C* **2017**, *121* (31), 16831−16844.

(34) Flikkema, E.; Bromley, S. A New Interatomic Potential for Nanoscale Silica. *Chem. Phys. Lett.* **2003**, *378* (5−6), 622−629.

(35) Pedone, A.; Malavasi, G.; Menziani, M. C.; Segre, U.; Musso, F.; Corno, M.; Civalleri, B.; Ugliengo, P. FFSiOH: A New Force Field for Silica Polymorphs and Their Hydroxylated Surfaces Based on Periodic B3LYP Calculations. *Chem. Mater.* **2008**, *20* (7), 2522−2531.

(36) Macià Escatllar, A.; Ugliengo, P.; Bromley, S. T. Modeling Hydroxylated Nanosilica: Testing the Performance of ReaxFF and FFSiOH Force Fields. *J. Chem. Phys.* **2017**, *146* (22), 224704.

(37) Lewis, G V; Catlow, C R A Potential Models for Ionic Oxides. *J. Phys. C: Solid State Phys.* **1985**, *18* (6), 1149−1161.

(38) Walker, A. M.; Wright, K.; Slater, B. A Computational Study of Oxygen Diffusion in Olivine. *Phys. Chem. Miner.* **2003**, *30* (9), 536−545.

(39) Schröder, K.-P.; Sauer, J.; Leslie, M.; Richard, C.; Catlow, A.; Thomas, J. M. Bridging Hydrodyl Groups in Zeolitic Catalysts: A Computer Simulation of Their Structure, Vibrational Properties and Acidity in Protonated Faujasites (H-Y Zeolites). *Chem. Phys. Lett.* **1992**, *188* (3−4), 320−325.

(40) Woodley, S. M. Structure Prediction of Ternary Oxide Sub-Nanoparticles. *Mater. Manuf. Processes* **2009**, *24* (3), 255−264.

(41) Mauney, C. M.; Lazzati, D. The Formation of Astrophysical Mg-Rich Silicate Dust. *Mol. Astrophys.* **2018**, *12*, 1−9.

(42) Sanders, M. J.; Leslie, M.; Catlow, C. R. A. Interatomic Potentials for SiO_2. *J. Chem. Soc., Chem. Commun.* **1984**, *19*, 1271.

(43) Li, R.; Cheng, L. Structural Determination of $(Al_2O_3)_n$ (N = 1−7) Clusters Based on Density Functional Calculation. *Comput. Theor. Chem.* **2012**, *996*, 125−131.

(44) Oueslati, I.; Kerkeni, B.; Bromley, S. T. Trends in the Adsorption and Reactivity of Hydrogen on Magnesium Silicate Nanoclusters. *Phys. Chem. Chem. Phys.* **2015**, *17* (14), 8951−8963.

(45) Kerkeni, B.; Bromley, S. T. Competing Mechanisms of Catalytic H_2 Formation and Dissociation on Ultrasmall Silicate Nanocluster Dust Grains. *Mon. Not. R. Astron. Soc.* **2013**, *435* (2), 1486−1492.

(46) Bromley, S. T.; Moreira, I. D. P. R. R.; Neyman, K. M.; Illas, F. Approaching Nanoscale Oxides: Models and Theoretical Methods. *Chem. Soc. Rev.* **2009**, *38* (9), 2657−2670.

(47) Chiang, C. M.; Zegarski, B. R.; Dubois, L. H. First Observation of Strained Siloxane Bonds on Silicon Oxide Thin Films. *J. Phys. Chem.* **1993**, *97* (27), 6948−6950.

(48) Hirshfeld, F. L. Bonded-Atom Fragments for Describing Molecular Charge Densities. *Theor. Chim. Acta* **1977**, *44* (2), 129−138.

(49) Viñes, F.; Lamiel-Garcia, O.; Illas, F.; Bromley, S. T. Size Dependent Structural and Polymorphic Transitions in ZnO: From Nanocluster to Bulk. *Nanoscale* **2017**, *9* (28), 10067−10074.

(50) Aguado, A.; López, J. M. Structures and Stabilities of CaO and MgO Clusters and Cluster Ions: An Alternative Interpretation of the Experimental Mass Spectra. *J. Phys. Chem. B* **2000**, *104* (35), 8398−8405.

(51) Malcolm, W.; Chase, J. *NIST-JANAF Thermochemical Tables*; 4th ed.; American Chemical Society: Washington, D.C., 1998.

(52) Zaitsev, A. I.; Arutyunyan, N. A.; Shaposhnikov, N. G.; Zaitseva, N. E.; Burtsev, V. T. Experimental Study and Modeling of the Thermodynamic Properties of Magnesium Silicates. *Russ. J. Phys. Chem.* **2006**, *80* (3), 335−344.

(53) Dong, R.; Chen, X.; Wang, X.; Lu, W. Structural Transition of Hexagonal Tube to Rocksalt for $(MgO)_{3n}$, $2 \leq n \leq 10$. *J. Chem. Phys.* **2008**, *129* (4), 044705.

(54) Chen, M.; Felmy, A. R.; Dixon, D. A. Structures and Stabilities of $(MgO)_n$ Nanoclusters. *J. Phys. Chem. A* **2014**, *118* (17), 3136−3146.

(55) Krasnokutski, S. A.; Rouillé, G.; Jäger, C.; Huisken, F.; Zhukovska, S.; Henning, T. Formation of Silicon Oxide Grains at Low Temperatures. *Astrophys. J.* **2014**, *782* (1), 15.

(56) Zhukovska, S.; Dobbs, C.; Jenkins, E. B.; Klessen, R. S. Modeling Dust Evolution in Galaxies with a Multiphase, Inhomogeneous ISM. *Astrophys. J.* **2016**, *831* (2), 147.

(57) Molster, F. J.; Waters, L. B. F. M.; Tielens, A. G. G. M. G. M.; Barlow, M. J. Crystalline Silicate Dust around Evolved Stars. *Astron. Astrophys.* **2002**, *382* (1), 222−240.

(58) Chiar, J. E.; Tielens, A. G. G. M. Pixie Dust: The Silicate Features in the Diffuse Interstellar Medium. *Astrophys. J.* **2006**, *637* (2), 774−785.

(59) Gail, H.-P. Chemical Reactions in Protoplanetary Accretion Disks. IV. Multicomponent Dust Mixture. *Astron. Astrophys.* **1998**, *332*, 1099−1122.

(60) Draine, B. T. Interstellar Dust Grains. *Annu. Rev. Astron. Astrophys.* **2003**, *41* (1), 241−289.

(61) De La Pierre, M.; Orlando, R.; Maschio, L.; Doll, K.; Ugliengo, P.; Dovesi, R. Performance of Six Functionals (LDA, PBE, PBESOL, B3LYP, PBE0, and WC1LYP) in the Simulation of Vibrational and Dielectric Properties of Crystalline Compounds. The Case of Forsterite Mg_2SiO_4. *J. Comput. Chem.* **2011**, *32* (9), 1775−1784.

(62) Suto, H.; Sogawa, H.; Tachibana, S.; Koike, C.; Karoji, H.; Tsuchiyama, A.; Chihara, H.; Mizutani, K.; Akedo, J.; Ogiso, K.; et al. Low-Temperature Single Crystal Reflection Spectra of Forsterite. *Mon. Not. R. Astron. Soc.* **2006**, *370* (4), 1599−1606.

(63) Jäger, C.; Molster, F. J.; Dorschner, J.; Henning, T.; Mutschke, H.; Waters, L. B. F. M.; Jäger, C.; Molster, F. J.; Dorschner, J.; Henning, T.; Mutschke, H.; Waters, L. B. F. M.; Jäger, C.; Molster, F. J.; Dorschner, J.; et al. Steps toward Interstellar Silicate Mineralogy. IV. The Crystalline Revolution. *Astron. Astrophys.* **1998**, *916*, 904−916.

(64) Haertelt, M.; Fielicke, A.; Meijer, G.; Kwapien, K.; Sierka, M.; Sauer, J. Structure Determination of Neutral MgO Clusters—Hexagonal Nanotubes and Cages. *Phys. Chem. Chem. Phys.* **2012**, *14* (8), 2849.

(65) Goumans, T. P. M.; Bromley, S. T. Hydrogen and oxygen adsorption on a nanosilicate − a quantum chemical study. *Mon. Not. R. Astron. Soc.* **2011**, *414*, 1285−1291.